Advanced Composites and Hybrid Materials (2023) 6:36
https://doi.org/10.1007/s42114-022-00621-0

RESEARCH

In situ enhancing thermal and mechanical properties of novel green WPAI nanocomposite membrane via artificially cultivated biomass-based diatom frustules

Yunu Shi[1] · Bin Li[1,2] · Xiaofang Jiang[1] · Chuanyong Yu[3] · Tao Li[1] · Haoyang Sun[1] · Shiwei Chen[1] · Dandan Li[1] · Dazhi Sun[1]

Received: 17 July 2022 / Revised: 4 December 2022 / Accepted: 28 December 2022 / Published online: 9 January 2023

Abstract

Water-based polyamide-imide (WPAI) resin has received extensive attention due to its greenness, safety, and favorable comprehensive properties. However, its low degree of molecular chain crosslinking results in poor heat resistance and mechanical strength, which seriously restricts its application as a matrix material for composite membranes. In this work, WPAI composite membranes were fabricated via the incorporation of artificially cultured diatom frustules (DFs), a biomass-based silicon dioxide material with a 3D penetration network structure. The prepared DFs@WPAI nanocomposite membranes are a novel green water–based material, which notably minimizes the utilization of toxic organic solvents. Moreover, the DFs-5@WPAI nanocomposite membrane after systematic optimization of structure and composition exhibits superior thermal stability (maximum servicing temperature of 514 °C) and mechanical strength (especially hardness of 0.39 GPa), which is comparable to those of the organic solvent-based composite membranes. The strengthening mechanisms of the DFs@WPAI nanocomposite membranes are attributed to the dual effects of physical riveting and in-situ chemical bonding between the DFs and the WPAI resin.

Keywords Green water–based nanocomposite membrane · Biomass-based diatom frustules · 3D penetration network structure · Physical riveting · In situ chemical bonding

1 Introduction

Polyamide-imide resin (PAI) has excellent thermal stability, mechanical strength, and chemical inertness properties because of the large number of five-membered heterocycles and aromatic rings in the skeleton structure [1–4]. Therefore, the composite membranes prepared using PAI resin as a film-forming phase are extensively utilized for the surface protection of metal materials to manipulate the thermodynamic, tribological, and corrosion properties [5–8].

In recent years, the continuous depletion of fossil resources and the increasing attention to environmental protection have triggered the research activities related to environmentally friendly polymer materials [9, 10]. Water-based PAI (WPAI) with water as the dispersion medium has attracted extensive attention from researchers because of its greenness, low toxicity, and safety [11, 12]. However, the WPAI resin is synthesized by introducing hydrophilic or ionic groups as emulsifiers into the PAI molecular chain. These polar groups destroy the structural integrity of the molecular chain [1, 13], resulting in a lower cross-linking degree of the resin, further leading to the deterioration of heat resistance and mechanical strength [14, 15].

Doping appropriate functional micro/nano additives is a remarkably effective way to optimize the thermal and mechanical properties of the water-based resin. After performing systematic research, it was concluded that the additives can be

✉ Bin Li
lbyxzh@126.com

✉ Xiaofang Jiang
jiangxflb@sina.com

✉ Dazhi Sun
sundz@sustech.edu.cn

[1] Guangdong Provincial Key Laboratory of Functional Oxide Materials and Devices, Department of Materials Science and Engineering, Southern University of Science and Technology, Shenzhen 518055, China

[2] China Merchants Marine Equipment Research Institute Co., Ltd., Shenzhen 518063, China

[3] Institute of Advanced Wear & Corrosion Resistant and Functional Materials, Jinan University, Guangzhou 510632, China

classified as follows: carbon-based nanoadditives (graphene oxide) [16, 17], the metal sulfides (CdS, Ag_2S) [18, 19], the rare earth compounds (LaF_3, CeF_3) [11, 20, 21], and the biomass-based diatom frustules (DFs) [22, 23] and diatomites [24]. Compared to the expensive carbon-based nanoadditives, highly toxic heavy metal sulfides, and rare earth compounds with limited storage, biomass-based DFs and diatomites are derived from siliceous cell walls of unicellular diatom, the source of which is environment-friendly and reproducible [25]. At the same time, because of the special three-dimensional (3D) penetrating multi-porous structure, the DFs have a larger specific surface area than the solid granular additives [26, 27] and diatomites [28], which is conducive to increasing the contact area between them and the resin. In addition, the DFs have outstanding temperature tolerance [23, 29], which is of great value in optimizing the thermal stability of nanocomposite membranes.

Another interesting DF feature is its super-hydrophilicity, which is due to the synergistic effect of the nano structure and the high-density silanol anion on the pore surface [30, 31]. In view of this, the strong physicochemical interactions may be formed between the DFs and the active hydrophilic functional groups of the WPAI resin to further modify the interfacial bonding strength between them, in order to optimize the thermal and mechanical properties of the DFs@WPAI nanocomposite membrane.

Based on the above research background, the in situ synthesis of the WPAI resin on the surface of hierarchical pores in the DFs was carried out to prepare novel green biomass-modified water-based nanocomposite membranes. The controllable preparation technology and optimization design criteria for the new green DFs-modified water-based composites were systematically identified by exploring the variation law of the thermal and mechanical properties of nanocomposite membranes. The interface bonding mode and synergistic mechanism between the DFs and the WPAI resin were also determined.

2 Experimental

2.1 Materials

WPAI resin was purchased from Beijing Sino-rich tech co., Ltd. (Beijing, China). The DFs were obtained from calcined and purified diatoms artificially cultured by Tali Energy Co., Ltd. (Shenzhen, Guangdong, China). The deionized water was prepared in the laboratory.

2.2 Preparation of water-based DFs@WPAI nanocomposite membrane

The preparation process for the nanocomposite membrane is shown in Fig. 1. In the first step of the DFs preparation, the DFs were calcined for 2 h at 600 °C. Then, the calcined DFs were etched with hydrochloric acid (0.1 mol/L) three times to remove impurities; specifically, the DFs were placed in hydrochloric acid and stirred with a magnet for 10 min and further vacuum filtered. After that, the DFs were washed with deionized water three times and then transferred to a heated blast drying box and kept for 2 h at 150 °C to remove moisture. Finally, the DFs were transferred to a ball mill tank for grinding treatment at 300 rpm for 4 h.

The second step refers to the preparation of the composite slurry. By adjusting the relative content of each component (DFs, WPAI resin, and deionized water), the total solid content was configured to be 9.5%. The percentages of DFs occupying the total solid mass were 0%, 1%, 3%, 5%, 7%,

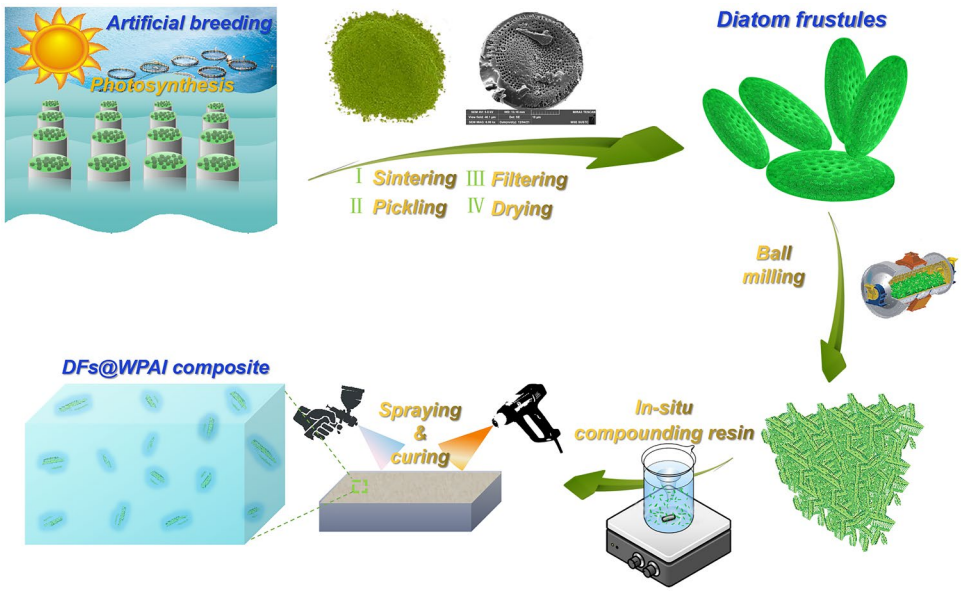

Fig. 1 Fabrication process of DFs@WPAI nanocomposite membranes

and 9% of DFs@WPAI nanocomposite slurry, which were referred to as DFs-0@WPAI, DFs-1@WPAI, DFs-3@WPAI, DFs-5@WPAI, DFs-7@WPAI, and DFs-9@WPAI nanocomposites, respectively. Using the preparation of 100 g of DFs-1@WPAI nanocomposite slurry as an example, 0.095 g of DFs, 36.667 g of WPAI resin, and 63.238 g of deionized water were first weighed out. Then, 0.095 g of DFs was added to 31.619 g of deionized water and mechanically stirred for 1.5 h to obtain a DF suspension. Furthermore, 36.667 g of WPAI resin was added to 31.619 g of deionized water and mechanically stirred for 0.5 h. The prepared water-based DF suspension was then gradually added dropwise and further fully stirred for 6.5 h to obtain a uniform and stable dispersion of the DFs@ WPAI nanocomposites.

The third step involved spraying and curing. The substrate (#45 steel block) was successively polished via 240 and 400 mesh sandpaper and then transferred to absolute ethanol for ultrasonic cleaning for 10 min. The slurry was evenly sprayed on the surface of the substrate via a spray gun. During the spraying process, the gun pressure was 0.3 MPa, the distance between the gun head and the substrate surface was about 35 cm, and the inclination angle was 45°. When the spraying process was over, all samples were transferred to a hot oven for curing (heating from room temperature to 80 °C, holding time of 6 h; heating to 150 °C, holding time of 3 h; heating to 270 °C, holding time of 1 h).

2.3 Characterization

The morphology of the DFs was characterized using a field emission scanning electron microscope (FESEM, TESCAN MIRA3, Czech; an acceleration voltage of 15.0 kV). The size of the DFs was determined using a nanoparticle size analyzer (HORIBA, Japan). The nitrogen adsorption isotherm curve of DFs was obtained by a surface adsorption analyzer (ASAP2020, USA) at 77 K, and the specific surface area was calculated by Brunauer-Emmett-Teller model. The chemical composition and structure of the DFs were analyzed by an X-ray photoelectron spectrometer (XPS, Escalab Xi+, UK; X-ray source: Al-Kα 1486.6 eV), Fourier transform infrared spectrometer (FTIR, Spotlight I2000i, USA), and X-ray diffractometer (XRD, Rigaku Smartlab, Japan; nickel-filtered Cu-Kα radiation, $\lambda = 0.154$ nm; 40 kV, 40 mA). The surface and cross-sectional morphology of the DFs@WPAI nanocomposite membranes was characterized by field emission scanning electron microscope (FESEM, TESCAN MIRA3, Czech), 3D profiler (Countor GT K, USA), atomic force microscope (AFM, Dimension Edge, USA), and focused ion beam (FIB, Helios 600i, USA). The thermal properties of the DFs@WPAI nanocomposite membranes were determined by a thermogravimetric analyzer (TGA, Mettler, Switzerland) at a heating rate of 10 °C/min under nitrogen atmosphere with a temperature ranging from 50 to 800 °C. The mechanical properties of the DFs@WPAI nanocomposite membranes were tested by a nanomechanical indenter (Hysitron TI950, USA), while the loading speed was 1000 μN/s, the maximum load was 5000 μN, and the maximum load retention time was 2 s. The interface composition between the DFs and WPAI resin was analyzed by virtue of high-resolution transmission electron microscopy (HRTEM, TECNAI G2F30, USA), XPS (Escalab Xi+, UK), and FTIR (Spotlight I2000i, USA).

3 Results and discussion

3.1 Composition and structure of DFs particles and water-based nanocomposite membranes

The DFs have a 3D penetration network structure (Fig. 2a), and the size of the DFs particles has a certain distribution range, with an average size of around 831.07 nm (Fig. 2b). Compared with solid granular additives [27, 32], the DFs have a larger specific surface area of 100.64 ($m^2 \cdot g^{-1}$) (Fig. 2c), which can considerably increase the contact area between additives and resins and further modify the interfacial bonding strength between the components [33–36].

The XPS analysis demonstrated that DFs are mainly composed of elements Si and O (Fig. 2d–f). The percentages of Si and O are 29.28 at.% and 61.73 at.%, respectively (the ratio of Si to O is about 0.5). Based on the XRD results (Fig. 2g), it can be concluded that the DF structure has a good match with that of the SiO_2 quartz. The infrared analysis results [37, 38] showed that 1098 cm^{-1} corresponds to the anti-symmetric stretching vibration peak of Si-O-Si, 798 cm^{-1} corresponds to the symmetric stretching vibration peak of Si-O-Si, and 472 cm^{-1} corresponds to the flexural vibration peak of Si-O-Si (Fig. 2h). Thus, these data again suggest that the chemical composition of the DFs is similar to that of SiO_2. In addition, 1631 cm^{-1} corresponds to the H-O-H flexural vibration peak, and 3448 cm^{-1} corresponds to the antisymmetric stretching vibration peak of -OH [30, 39], which indicates that the Si-OH structure is formed on the surface of the DFs. Furthermore, Si-OH groups give the DFs excellent hydrophilicity, which is conducive to the formation of stronger chemical bonds between the DFs and WPAI resin.

On the other hand, the thermogravimetric analysis of the DFs (Fig. 2i) showed that when the temperature rises to 900 °C, the DFs only lose 7.03% of weight, which may be caused by the desorption of the adsorbed water or other impurity gas on the surface of the DFs under high-temperature conditions.

Systematic analysis of the micro-distribution of components and interface composition between the DFs and WPAI resin was conductive to revealing the interface interaction mode. In situ HRTEM analysis observed the interfacial component bonding in the water-based DF@WPAI nanocomposites (Fig. 3). It should be noted that C and N are the

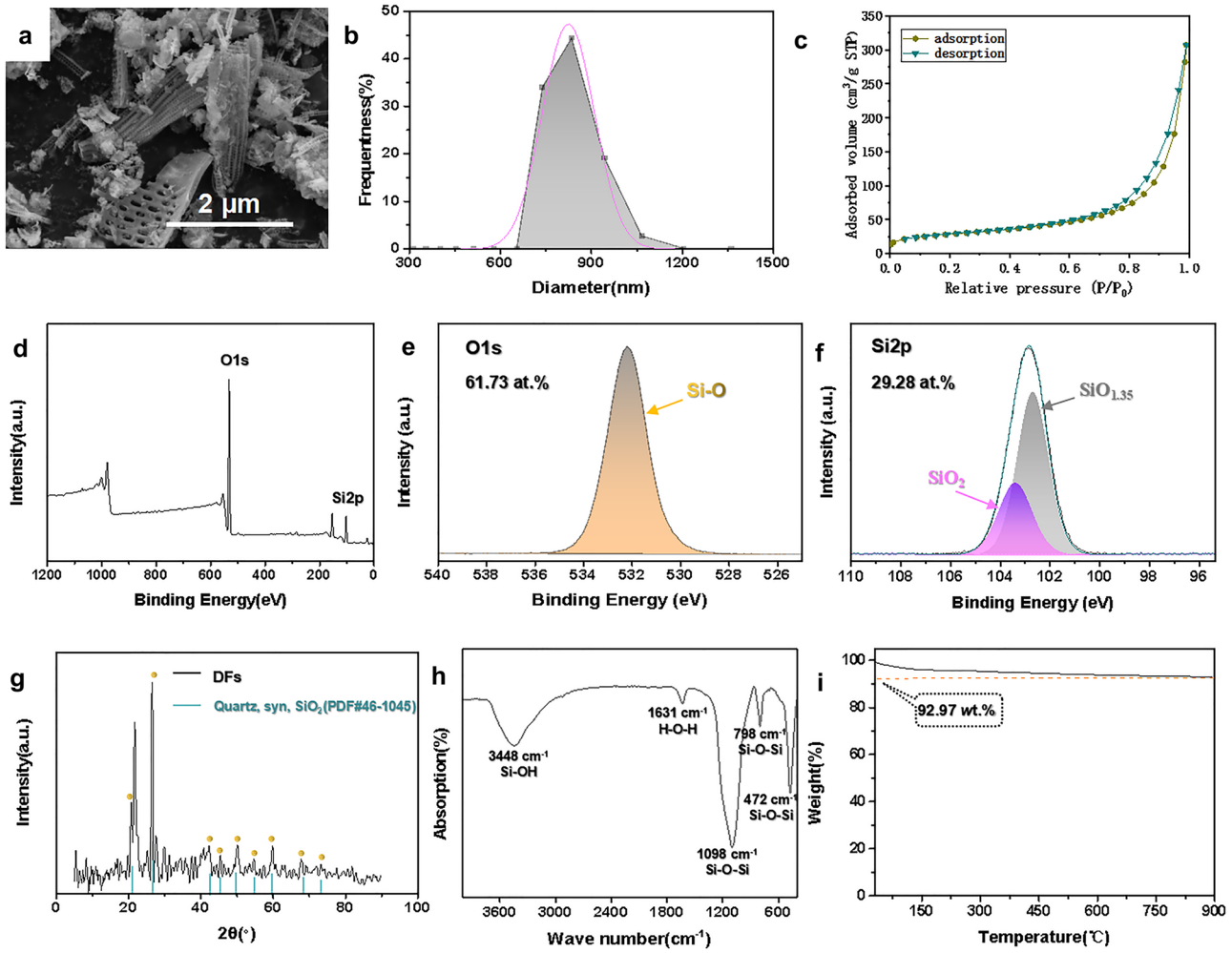

Fig. 2 Basic physicochemical parameters of the DFs: **a** SEM image; **b** size; **c** N_2 adsorption–desorption isotherm curve; **d**–**f** XPS spectrum; **g** XRD pattern; **h** FT-IR spectra; **i** thermal properties

characteristic elements of the WPAI resin, Si and O are the characteristic elements of the DFs, and their distribution positions correspond to the WPAI resin and DFs, respectively. From the morphology of random DFs (Fig. 3a, b) and distribution of characteristic DF and WPAI resin elements (Fig. 3c–f), it is clear that the WPAI resin is evenly distributed where the DFs are present, which indicates that it may fill the DF pores or encapsulate them to form the DF@WPAI nanocomposite with an interpenetrating network structure. Therefore, it can effectively limit the migration of WPAI resin molecular chains to further enhance the interfacial bonding strength between components by taking advantage of this physical anchoring effect of the DFs (Fig. 3g). In addition, it should be emphasized that the samples tested above were prepared after sufficient dilution and ultrasonic shock in deionized water, although the results showed that the WPAI resin was still firmly attached to the surface and interior of the DFs. Since the WPAI resin has excellent water dispersibility [11, 21], it shows that the combination mechanism of the DFs and the resin is not a simple physical adsorption, and there may be some type of chemical bonding.

Relevant qualitative analyses of the chemical composition of the interfaces between the WPAI and DFs were systematically carried out in the nanocomposite membrane (Fig. 4). On one hand, Fig. 4a represents the infrared absorption peaks of the WPAI resin, DFs, and DFs-5@WPAI nanocomposites. The wave numbers and the corresponding chemical groups marked on the pink curve confirm the basic compositions and structure of the WPAI resin, which has been verified in our previous work [40]. The wave numbers and the corresponding chemical groups of the DFs marked on the dark green curve were analyzed in detail in Fig. 2h. Moreover, the gray curve of the DFs-5@WPAI composites includes all DFs and WPAI resin absorption peaks (marked at the same wave number position). Among them, it is worth noting that the wavenumber in the range of 1100 to 1000 cm^{-1} corresponds

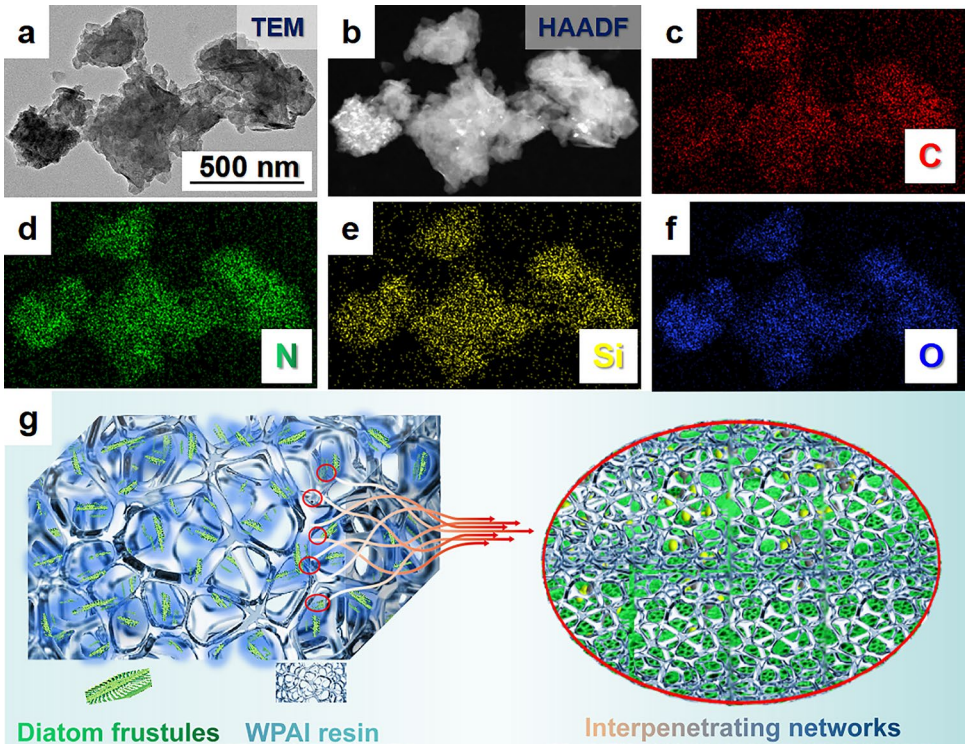

Fig. 3 Microscopic distribution of the DFs in WPAI resin in fully diluted water-based nanocomposite slurry: **a**, **b** TEM image; elemental mapping of **c** C, **d** N, **e** Si, and **f** O; **g** compounding model

to the infrared absorption peak of Si-O-Si, which appears in the peaks corresponding to the DFs and DFs-5@WPAI nanocomposites. Surprisingly, the corresponding infrared absorption peaks of DFs-5@WPAI nanocomposites appeared three new absorption peaks at the wavenumbers of 1087 cm^{-1}, 1051 cm^{-1}, and 1016 cm^{-1}, respectively (Fig. 4b), which have been documented that the above three absorption peaks correspond to the characteristic absorption peaks of Si-O-Si [41], Si-O-CH_3 [41], and [-Si$(CH_3)_2$-O-] [42, 43], which indicates that the novel chemical bonds are formed between the DFs and the WPAI resin.

Furthermore, Fig. 4c shows the full spectrum analysis using XPS of the DFs-5@WPAI nanocomposites, DFs, and pure resin. Figure 4d corresponds to the fine spectrum analysis of the Si element in the DFs, and Fig. 4e represents the fine spectrum analysis of the Si element in the DFs-5@WPAI nanocomposites. The full spectrum analysis in Fig. 4c shows that the WPAI resin is mainly composed of O, N, and C; the DFs are composed of O, C, and Si; and the DFs-5@WPAI nanocomposites are composed of O, N, C, and Si. In order to further clarify the chemical state of Si in the composite, it is necessary to systematically compare and analyze the high resolution spectra of Si in the DFs and DFs-5@WPAI nanocomposites. The chemical composition of DFs includes two forms of SiO_2 (~103.40 eV) and $SiO_{1.35}$ (~102.70 eV) (Fig. 4d) [44]. Among them, the appearance of $SiO_{1.35}$ is due to the insufficient coordination of Si atoms exposed in the outermost DF layer, which may be caused by the existence of Si-OH groups (referring to the analysis in Fig. 2h). The high-resolution spectra of Si in the DFs-5@WPAI nanocomposites in Fig. 4e illustrate that there are two new peaks of [-Si(OCH_3)-O-Si(OCH_3)-] $2p^{3/2}$ (~102.92 eV) [45] and [-Si$(CH_3)_2$-O-]$_n$ $2p^{3/2}$ (~101.79 eV) [46] in addition to the SiO_2 peak. The above analytical results also revealed the formation of the chemical bonding between the DFs and WPAI resin.

3.2 Morphology of water-based nanocomposite membranes

Figure 5 shows the surface and cross-section characteristics of the DFs-5@WPAI nanocomposite membranes. Combined with the surface and cross-sectional topographies and the distribution of characteristic elements (Fig. 5a–c, f, g), it is evident that the DFs are evenly dispersed in the WPAI resin, that is, the resin fully envelops the DFs. According to the AFM phase diagrams (Fig. 5d, e), the surface of the WPAI@DF nanocomposite membrane has a bright and dark appearance, in which the darker positions correspond to the softer resin, and the brighter positions correspond to the harder DFs. A mild light–dark transition at the interface between the DFs and WPAI resin indicates that there is no obvious phase separation model, suggesting that the porous structure of the DFs is filled with WPAI resin to form compact nanocomposites [47], which verifies the previous speculation for Fig. 3. Based on the above analysis, it can be concluded that there is a relatively stable physical interlocking between the DFs and WPAI resin, giving full play to the synergistic compound effect between the two (the strengthening effect of the DFs and the cohesive effect of the resin).

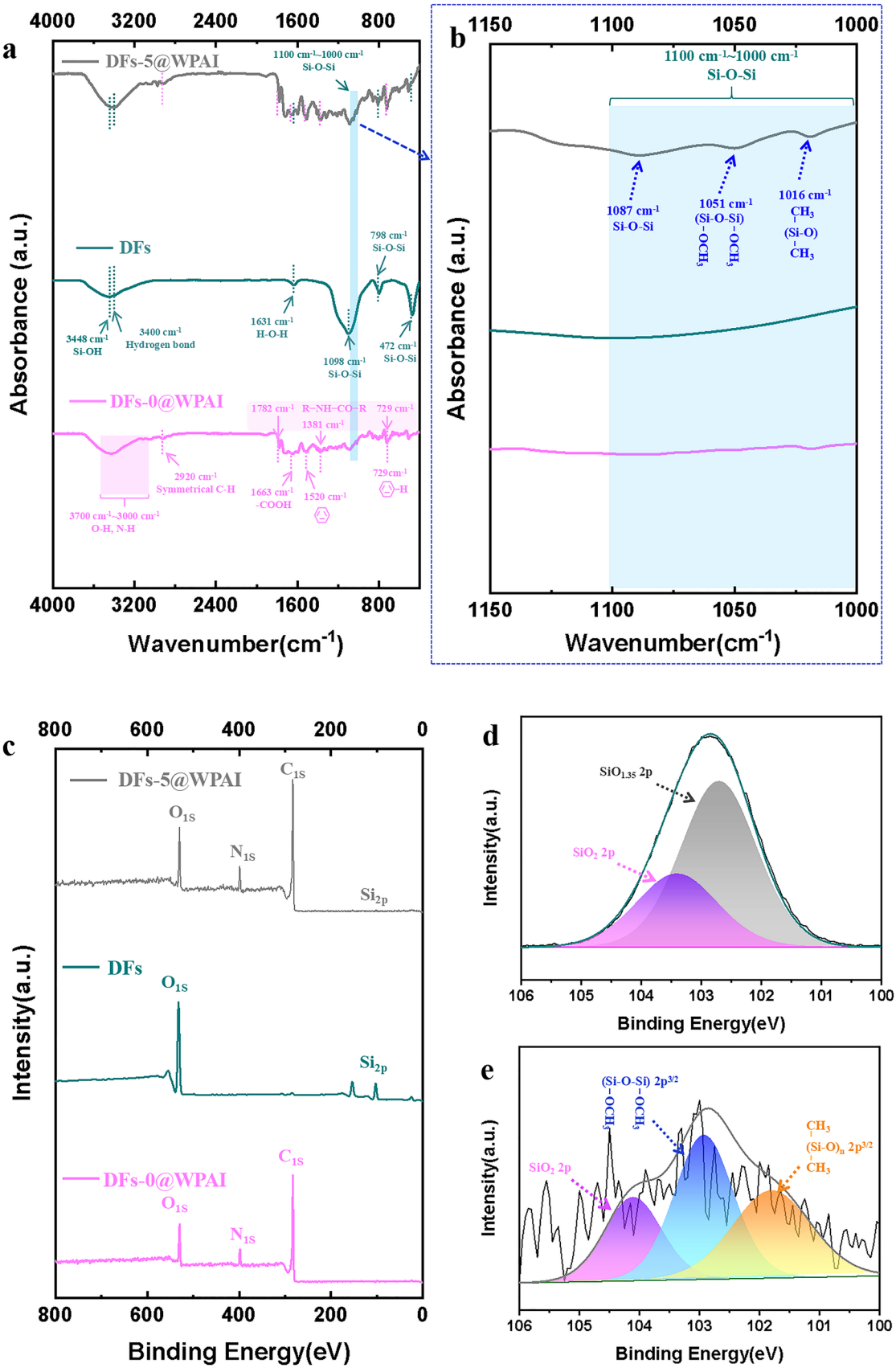
a
DFs-5@WPAI
1100 cm-1~1000 cm-1
Si-O-Si
DFs
798 cm-1
Si-O-Si
3448 cm-1
Si-OH
3400 cm-1
Hydrogen bond
1631 cm-1
H-O-H
1098 cm-1
Si-O-Si
472 cm-1
Si-O-Si
DFs-0@WPAI
1782 cm-1
R–NH–CO–R
1381 cm-1
729 cm-1
2920 cm-1
Symmetrical C-H
729cm-1
-H
1663 cm-1
-COOH
1520 cm-1
3700 cm-1~3000 cm-1
O-H, N-H
Absorbance (a.u.)
Wavenumber(cm-1)
4000
3200
2400
1600
800
b
1150
1100
1050
1000
1100 cm-1~1000 cm-1
Si-O-Si
1087 cm-1
Si-O-Si
1051 cm-1
(Si-O-Si)
1016 cm-1
CH3
(Si-O)
CH3
Absorbance (a.u.)
Wavenumber(cm-1)
c
DFs-5@WPAI
C1S
O1S
N1S
Si2p
DFs
O1S
Si2p
DFs-0@WPAI
C1S
O1S
N1S
Intensity(a.u.)
Binding Energy(eV)
800
600
400
200
0
d
SiO1.35 2p
SiO2 2p
Intensity(a.u.)
Binding Energy(eV)
106
105
104
103
102
101
100
e
(Si-O-Si) 2p3/2
SiO2 2p
CH3
(Si-O)n 2p3/2
CH3
Intensity(a.u.)
Binding Energy(eV)

◂**Fig. 4** Chemical composition of interfaces between the WPAI and DFs: **a** FT-IR spectra for the DFs-5@WPAI composites, DFs, and WPAI resin; **b** Partial enlargement of the infrared spectrum from **a**; **c** wide-scan XPS spectrum analysis of the DFs-5@WPAI composites, DFs, and WPAI resin; **d** high-resolution Si 2p XPS spectrum of DFs; **e** high-resolution Si 2p XPS spectrum of the DFs-5@WPAI composites

3.3 Physicochemical and thermodynamic properties of the water-based WPAI@DFs nanocomposite membranes

Table 1 represents the basal physicochemical properties of the WPAI@DFs nanocomposite membranes. Owing to the inevitable errors in the spraying and the thickness-measuring processes, the thickness has a range of fluctuations, which are all reasonable compared to the reported literature [11, 14, 48]. In addition, it is apparent that the surface roughness of the series of the nanocomposite membranes is approximately equal to 0.070 μm, which is nearly two orders of magnitude lower than that of the reported water-based nanocomposite membranes [14, 20]. The ultra-high flatness can effectively reduce the local compressive stress on coated metal surfaces to further notably enhance the protective capability of the composite membranes. At the same time, the adhesion of the composite membrane was of grade 1, the flexibility was 1 mm, and the impact resistance was equal to approximately 120 cm, which meets or exceeds the corresponding performance standards of the organic solvent-based composite membranes [9, 49]. In summary, the above analytical results demonstrate that the large application potential of this type of composite membrane will effectively promote the development of the composite membrane towards a green and renewable direction.

Thermal analysis is an effective method to measure the thermal stability of polymer matrix composites [15, 17, 50]. The TGA and DTG analyses of the nanocomposite membranes after the crosslinking and interaction are shown in Fig. 6 and Table 2. The compositional change in the composite membranes has a noticeable effect on the thermal properties (Fig. 6a and Table 2). In the initial decomposition stage, as the content of DFs in the composite increases, the corresponding temperature (T_{10}) when the weight loss is 10% shows a gradual growth trend. Here, the T_{10} of WPAI is about 454 °C, the T_{10} of DFs-5@WPAI is about 473 °C, and the T_{10} of DFs-9@WPAI is about 482 °C, which is nearly 30 °C higher than the T_{10} of the pure resin matrix. This implies that the thermal stability of the composite membrane is obviously enhanced by compounding a small amount of DFs, and the superior temperature resistance of the green water-based nanocomposite membrane has an advantage in the thermal protection of the metal surface [51–53]. In addition, the temperature corresponding to the maximum

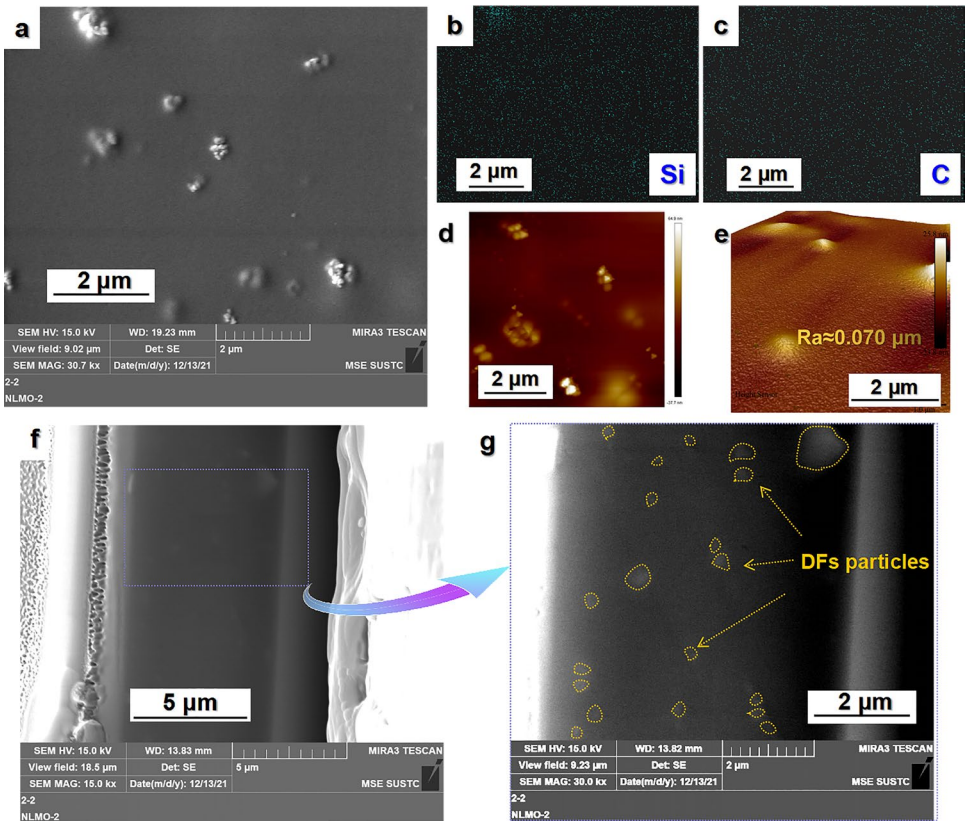

Fig. 5 Surface and cross-section morphology and composition distribution of the DF-5@WPAI nanocomposite membrane: **a** SEM image of surface; **b** elemental mapping of Si; **c** elemental mapping of C; **d**, **e** AFM image of surface; **f**, **g** SEM image of a cross-section

Table 1 Basal physicochemical properties of the DFs@WPAI nanocomposite membranes

Physical parameters	Thickness (μm)	Roughness (μm)	Adhesion (grade)	Flexibility (mm)	Impact resistance (cm)
Nanocomposite membrane	20.0±2.0	0.070±0.002	1	1	120

degradation rate (T_{max}) can be determined using the DTG diagram (Fig. 6b and Table 2). The T_{max} shows a gradually increasing trend with an increase in the DF content in the nanocomposite membrane, and the maximum degradation rate shows a gradually decreasing trend. This illustrates that with the progress of the thermal decomposition reaction, the compounding modification of the DFs postpones the depolymerization of WPAI molecules and further raises the T_{max} of the nanocomposite membranes.

Compared to the pure resin matrix, the detailed modification mechanisms for the thermal properties of the DFs@WPAI composite membranes are as follows: First, the DFs have a superior thermal stability (Fig. 2i), which contributes to optimizing the overall temperature tolerance of the composite membrane. Second, when the nanocomposite is in the form of a slurry, that is, when the DF particles with a 3D porous structure are combined with WPAI resin molecules, the molecular chains of the WPAI resin penetrate the DF particles and enter the DF holes. After the resin is solidified, the DFs can effectively restrict the movement of the molecular chains to further modify the temperature endurance of the composites. Simultaneously, the chemical bonds between the DFs and the resin can also helpfully consolidate the interfacial bonding strength between the components, which is beneficial to further optimize the thermal stability of the nanocomposite membrane.

3.4 Mechanical properties

The mechanical properties of the DFs@WPAI nanocomposite membranes are shown in Fig. 7. The hardness first increases and then decreases (Fig. 7a), reaching a maximum value of 0.39 GPa, which is comparable to that of organic solvent-based nanocomposite membranes [19, 49]. The plastic deformation first decreases and then increases (Fig. 7b), while the elastic modulus first increases and then decreases (Fig. 7c). Thus, the degree of plastic deformation of the composites is negatively correlated with the elastic modulus, which implies that the larger the elastic modulus of the nanocomposites, the stronger the deformation resistance, and the more difficult it is to reach the yield point of the material. Therefore, under the same load, the plastic deformation of the nanocomposites is smaller.

There are several reasons for the differences in hardness, plastic deformation, and elastic modulus variability in the nanocomposite membranes. On one hand, the reduction in the content of DFs is not conducive to fully exerting the enhancement effect of DFs on the nanocomposites. On the other hand, the excessive addition partly aggravates the agglomeration and the uniformity of the DFs in nanocomposites. Therefore, the deformation resistance of the composites is reduced, and the plastic deformation of the composites increases sharply. In addition, when the DFs are properly compounded (DFs-5@WPAI), the synergistic strengthening effect between the DFs and the resin is fully exerted [54].

Furthermore, the strengthening mechanism related to the mechanical properties of the nanocomposites can be stated as follows: when the resin is properly compounded with DFs, the hardness, plastic deformation resistance, and elastic modulus of the DFs-5@WPAI nanocomposite membrane are significantly optimized. In essence, it is attributed to the

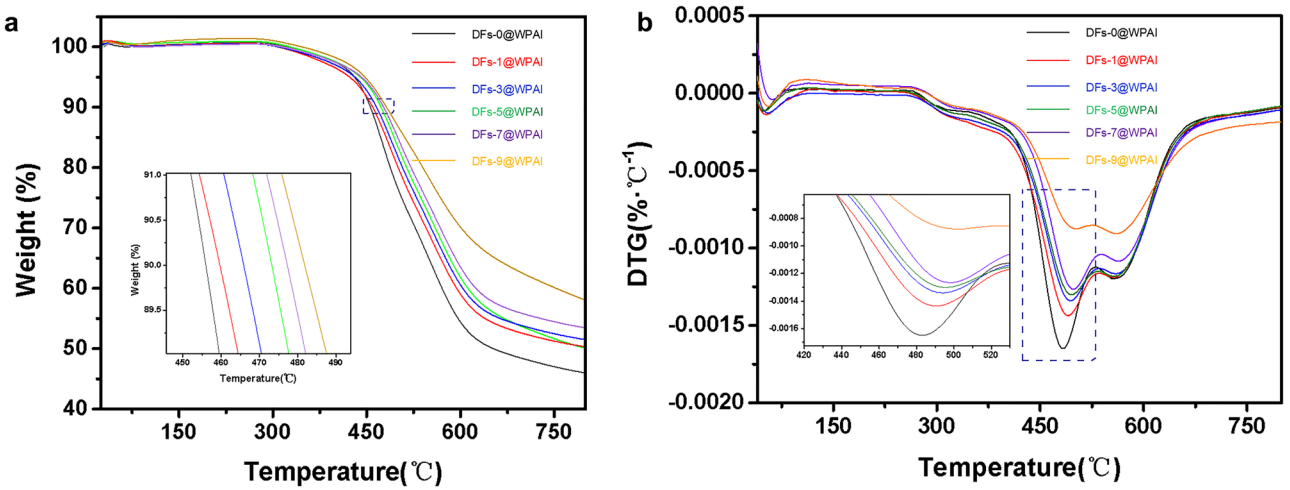

Fig. 6 Thermal properties of the DFs@WPAI nanocomposite membranes: **a** TGA curves; **b** DTG curves

Table 2 Thermal properties of the DFs@WPAI nanocomposite membranes

	DFs-0@WPAI	DFs-1@WPAI	DFs-3@WPAI	DFs-5@WPAI	DFs-7@WPAI	DFs-9@WPAI
T_{10}(°C)	454	459	466	473	477	482
T_{max}(°C)	482	489	492	496	499	502

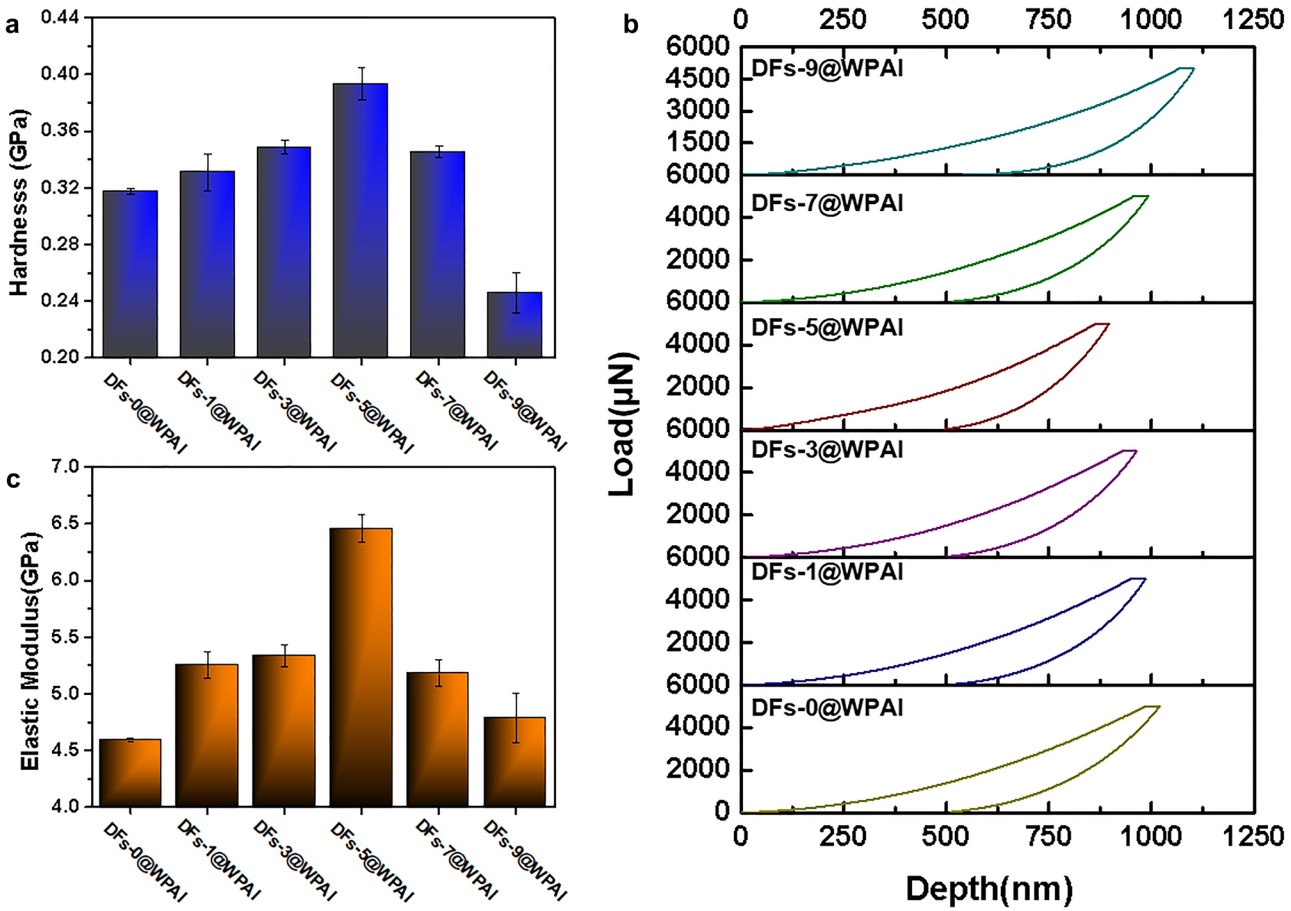

Fig. 7 Mechanical properties of the DFs@WPAI nanocomposite membranes: **a** hardness; **b** load–displacement curves; **c** elastic modulus

formation of the interpenetrating network structure between the DFs and the resin, meaning that this not only is due to the physical riveting and fixing effect between the DFs and the resin but also depends on the chemical bonding between the component interfaces.

4 Conclusion

The present study performed in situ optimization of thermal and mechanical properties of the green WPAI composite membranes with artificially cultivated DFs. The graft polymerization reaction between the DFs and WPAI resin forms an interpenetrating network structure, which radically limits the migration of resin molecular chains and significantly enhances the thermal stability and mechanical strength. This work contributes to promoting the practical application of green water-based DFs-modified nanocomposite membranes in the field of material surface protection. The specific conclusions are as follows: the water-based DFs-5@WPAI nanocomposite membranes are novel green composite materials with robust physicochemical properties and structural compactness; the combination mode of the DFs and WAPI resin is not just the physical adsorption, but also multiple chemical bonding; the water-based DFs-5@WPAI nanocomposites exhibit superior thermostability (the maximum servicing temperature of 514 °C) and mechanical strength (especially hardness of 0.39 GPa), showing significant application potential in replacing organic solvent-based nanocomposite membranes; the superior thermal and

mechanical properties of DFs-5@WPAI nanocomposites are attributed to the "dual function" of physical riveting and fixing effect, as well as the interfacial chemical bonding between the DFs and WPAI resin.

Author contribution Yunu Shi: conceptualization, preparation, resources, data analysis, supervision, writing—original draft. Bin Li: investigation, methodology, data analysis, sample preparation, writing, review, editing. Xiaofang Jiang: data curation, formal analysis. Chuanyong Yu: formal analysis. Tao Li: drawing, mechanism analysis. Haoyang Sun: data curation. Shiwei Chen: formal analysis. Dandan Li: data curation, supervision. Dazhi Sun: editing, supervision.

Funding This work received financial support from the Guangdong Provincial Key Laboratory Program (2021B1212040001), the Department of Science and Technology of Guangdong Province, the Shenzhen Science and Technology Innovation Committee (KQJSCX20180322152424539), the Southern University of Science and Technology and Taili Energy Co. Ltd., and the Postdoctoral Research Foundation of China (2021M691399).

Data availability The raw/processed data required to reproduce these findings cannot be shared at this time as the data also forms part of an ongoing study.

Declarations

Competing interests The authors declare no competing interests.

References

1. Liu Z, Cai Y, Song F, Li J, Zhang J, Sun Y, Luo G, Shen Q (2022) Study on chemical graft structure modification and mechanical properties of photocured polyimide. ACS Omega 7(11):9582–9593
2. Robertson GP, Guiver MD, Yoshikawa M, Brownstein S (2004) Structural determination of Torlon® 4000T polyamide–imide by NMR spectroscopy. Polymer 45(4):1111–1117
3. Çakir M, Akin E (2022) Characterization of carbon fiber-reinforced thermoplastic and thermosetting polyimide matrix composites manufactured by using various synthesized PI precursor resins. Compos B Eng 231:109559
4. Duan G, Liu S, Jiang S, Hou H (2019) High-performance polyamide-imide films and electrospun aligned nanofibers from an amide-containing diamine. J Mater Sci 54(8):6719–6727
5. Gong H, Yu C, Zhang L, Xie G, Guo D, Luo J (2020) Intelligent lubricating materials: a review. Compos B Eng 202:108450
6. Xi Z, Wan H, Chen L, Zhou H, Chen J (2022) Strengthening mechanism of in-situ synthesized Cu_2S nanoparticles on tribological performance of polyamide-imide bonded solid lubricating coatings. Prog Org Coat 166:106807
7. Zhou S, Xu T, Jin L, Song N, Ding P (2022) Ultraflexible polyamide-imide films with simultaneously improved thermal conductive and mechanical properties: design of assembled well-oriented boron nitride nanosheets. Compos Sci Technol 219:109259
8. Xu T, Zhou S, Cui S, Song N, Shi L, Ding P (2019) Three-dimensional carbon fiber-graphene network for improved thermal conductive properties of polyamide-imide composites. Compos B Eng 178:107495
9. Selim MS, Shenashen MA, El-Safty SA, Higazy SA, Selim MM, Isago H, Elmarakbi A (2017) Recent progress in marine foul-release polymeric nanocomposite coatings. Prog Mater Sci 87:1–32
10. Wang C, Liu S, Li M, Wang Z, Luo H, Fan W, Liu Z, Liu F, Wang H (2021) Novel environmentally friendly waterborne epoxy coating with long-term antiscaling and anticorrosion properties. Langmuir 37(31):9439–9450
11. Li B, Jiang X, Wan H, Chen L, Ye Y, Zhou H, Chen J (2018) Fabrication and tribological behaviors of a novel environmental friendly water-based PAI-PTFE-LaF_3 bonded solid lubricating composite coating. Tribol Int 121:400–409
12. Li B, Xv W, Liu P, Huang D, Zhou X, Zhao R, Li S, Liu Q, Jiang X (2021) Novel green lubricated materials: aqueous PAI-MoS_2-graphite bonded solid lubricating coating. Prog Org Coat 155:106225
13. Yao Y, Wang M, Wu H, Shen Y (2022) Synthesis of waterborne epoxy resin with diethanolamine-assisted succinimide for improving the strand integrity of polyimide filament. J Ind Text 51:8323S-8337S
14. Li B, Jiang X, Wan H, Chen L, Ye Y, Zhou H, Chen J (2019) Environment-friendly aqueous PTFE based bonded solid lubricating coatings: mechanical and tribological properties under diversified environments. Prog Org Coat 137:104904
15. Wang H, Xu J, Du X, Du Z, Cheng X, Wang H (2021) A self-healing polyurethane-based composite coating with high strength and anti-corrosion properties for metal protection. Compos B Eng 225:109273
16. Chathuranga H, Chandula Wasalathilake K, Marriam I, MacLeod J, Zhang Z, Bai R, Lei Z, Li Y, Liu Y, Yang H, Yan C (2021) Preparation of bioinspired graphene oxide/PMMA nanocomposite with improved mechanical properties. Compos Sci Technol 216:109046
17. Reyhani R, Zadhoush A, Tabrizi NS, Nazockdast H, Naeimirad M (2021) The influence of CNT-doped carbon aerogels on microstructural, rheological and mechanical properties of epoxy nanocomposites. Compos Sci Technol 215:109031
18. Agarwal S, Patidar D, Saxena NS (2013) Study on glass transition temperature and mechanical properties of cadmium sulfide/polystyrene nanocomposites. Polym Eng Sci 53(6):1223–1229
19. Ma Y, Zhao Z, Xian Y, Wan H, Ye Y, Chen L, Zhou H, Chen J (2019) Highly dispersed Ag_2S nanoparticles: in situ synthesis, size control, and modification to mechanical and tribological properties towards nanocomposite coatings. Nanomaterials 9(9):1308
20. Mazumder S, Metselaar HSC, Sukiman NL, Zulkifli NWM (2020) An overview of fluoride-based solid lubricants in sliding contacts. J Eur Ceram Soc 40(15):4974–4996
21. Li B, Jiang X, Wan H, Chen L, Ye Y, Zhou H, Chen J (2018) Optimum hydrophilic modification of lanthanum trifluoride nanoparticles and their application in enhancing tribological properties of eco-friendly water-based bonded solid lubricating coatings. Tribol Int 125:1–11
22. Li T, Sun H, Wu B, Han H, Li D, Wang JK, Zhang J, Huang J, Sun D (2020) High-performance polylactic acid composites reinforced by artificially cultured diatom frustules. Mater Des 195:109003
23. Zhang C, Sun J, Lyu S, Lu Z, Li T, Yang Y, Li B, Han H, Wu B, Sun H, Li D, Huang J, Sun D (2022) Poly(lactic acid)/artificially cultured diatom frustules nanofibrous membranes with fast and controllable degradation rates for air filtration. Adv Compos Hybrid Mater 5:1221-1232
24. Li X, Lin H, Jiang H, Zhang Y, Liu B, Sun Y, Zhao C (2021) Preparation and properties of a new bio-based epoxy resin/diatomite composite. Polym Degrad Stabil 187:109541
25. Rabiee N, Khatami M, Jamalipour Soufi G, Fatahi Y, Iravani S, Varma RS (2021) Diatoms with invaluable applications in nanotechnology, biotechnology, and biomedicine: recent advances. ACS Biomater Sci Eng 7(7):3053–3068
26. Reid A, Buchanan F, Julius M, Walsh PJ (2021) A review on diatom biosilicification and their adaptive ability to uptake other metals into their frustules for potential application in bone repair. J Mater Chem B 9(34):6728-6737

27. Feng G, Wang J, Boronat M, Li Y, Su JH, Huang J, Ma Y, Yu J (2018) Radical-facilitated green synthesis of highly ordered mesoporous silica materials. J Am Chem Soc 140(14):4770–4773
28. Huang J, Wu B, Lyu S, Li T, Han H, Li D, Wang JK, Zhang J, Lu X, Sun D (2021) Improving the thermal energy storage capability of diatom-based biomass/polyethylene glycol composites phase change materials by artificial culture methods. Sol Energy Mater Sol Cells 219:110797
29. Sun H, Li T, Lei F, Lyu S, Yang Y, Li B, Han H, Wu B, Huang J, Zhang C, Li D, Sun D (2021) Fast self-healing superhydrophobic thermal energy storage coatings fabricated by bio-based beeswax and artificially cultivated diatom frustules. ACS Appl Mater Interfaces 13(40):48088-48100
30. Lee J, Lee HA, Shin M, Juang LJ, Kastrup CJ, Go GM, Lee H (2020) Diatom frustule silica exhibits superhydrophilicity and superhemophilicity. ACS Nano 14(4):4755–4766
31. Sardo A, Orefice I, Balzano S, Barra L, Romano G (2021) Mini-review: potential of diatom-derived silica for biomedical applications. Appl Sci 11(10):4533
32. Lyu S, Wang Y, Han H, Ding C, Li D, Wang JK, Zhang J, Huang J, Sun D, Yu P (2021) Microstructure characterization and mechanical properties of Al-matrix composites reinforced by artificially-cultured diatom frustules. Mater Des 206:109755
33. Jia Z, Liu X, Zhou X, Zhou Z, Wu G (2022) A seed germination-inspired interface polarization augmentation strategy toward superior electromagnetic absorption performance. Compos Commun 34:101269
34. Liu Y, Jia Z, Zhan Q, Dong Y, Xu Q, Wu G (2022) Magnetic manganese-based composites with multiple loss mechanisms towards broadband absorption. Nano Res 15(6):5590–5600
35. Liu Y, Zhou X, Jia Z, Wu H, Wu G (2022) Oxygen Vacancy-induced dielectric polarization prevails in the electromagnetic wave-absorbing mechanism for Mn-based MOFs-derived composites. Adv Func Mater 32(34):2204499
36. Jia Z, Kong M, Yu B, Ma Y, Pan J, Wu G (2022) Tunable Co/ZnO/C@MWCNTs based on carbon nanotube-coated MOF with excellent microwave absorption properties. J Mater Sci Technol 127:153–163
37. Wu B, Lyu S, Han H, Li T, Sun H, Wang JK, Li D, Lei F, Huang J, Sun D (2021) Biomass-based shape-stabilized phase change materials from artificially cultured ship-shaped diatom frustules with high enthalpy for thermal energy storage. Compos B Eng 205:108500
38. Li T, Sun H, Han H, Zhang C, Li B, Huang J, Sun D (2022) Ultrafast bulk degradation of polylactic acid by artificially cultured diatom frustules. Compos Sci Technol 223:109410
39. Wu Z, Zhang C, Peng L, Wang X, Kong Q, Gu X (2018) Enhanced stability of MFI zeolite membranes for separation of ethanol/water by eliminating surface Si–OH groups. ACS Appl Mater Interfaces 10(4):3175–3180
40. Li B, Ye Y, Wan H, Chen L, Chen J (2017) Preparation and tribology properties of hydrophilic molybdenum disulfide bonded solid lubricating coatings. China Surf Eng 30(4):142–149
41. Manna AK, De PP, Tripathy DK, De SK, Peiffer DG (1999) Bonding between precipitated silica and epoxidized natural rubber in the presence of silane coupling agent. J Appl Polym Sci 74(2):389–398
42. Abdul Hamid ZA, Hong Fook L (2016) Synthesis and functionalization of silicone hydride copolymer with allyl methacrylate via hydrosilylation method. Adv Mat Res 1133:216–220
43. Raynaud P, Despax B, Segui Y, Caquineau H (2005) FTIR plasma phase analysis of hexamethyldisiloxane discharge in microwave multipolar plasma at different electrical powers. Plasma Processes Polym 2(1):45–52
44. Alfonsetti R, Lozzi L, Passacantando M, Picozzi P, Santucci S (1993) XPS studies on SiOx thin films. Appl Surf Sci S 70:222–225
45. Wagner CD, Passoja DE, Hillery HF, Kinisky TG, Six HA, Jansen WT, Taylor JA (1998) Auger and photoelectron line energy relationships in aluminum–oxygen and silicon–oxygen compounds. J Vac Sci Technol 21(4):933–944
46. Beamson G, Briggs D (1992) High Resolution XPS of organic polymers. The Scienta ESCA 300 database
47. Xu W, Wang W, Hao L, Liu H, Hai F, Wang X (2021) Synthesis and properties of novel triazine-based fluorinated chain extender modified waterborne polyurethane hydrophobic films. Prog Org Coat 157:106282
48. Li B, Jiang X, Sun H, Li T, Chen S, Lyu S, Zhang C, Yu C, Shi Y, Li D, Sun D (2021) Novel green waterborne polyurethane-polytetrafluoroethylene BSLCs: chemically optimized crosslinking extent for enhancing the mechanical and tribological properties. Prog Org Coat 161:106457
49. Wan H, Jia Y, Ye Y, Xu H, Cui H, Chen L, Zhou H, Chen J (2017) Tribological behavior of polyimide/epoxy resin-polytetrafluoroethylene bonded solid lubricant coatings filled with in situ-synthesized silver nanoparticles. Prog Org Coat 106:111–118
50. Ma R, Zhang H, Xu J, Sun L, Hayashi Y, Yoshida R, Shiomi J, Wang JX, Luo T (2022) Machine learning-assisted exploration of thermally conductive polymers based on high-throughput molecular dynamics simulations. Mater Today Phys 28:100850
51. Uyanna O, Najafi H (2020) Thermal protection systems for space vehicles: a review on technology development, current challenges and future prospects. Acta Astronaut 176:341–356
52. Yasir M, Ahmad F, Megat-Yusoff PSM, Ullah S, Jimenez M (2019) Quantifying the effects of basalt fibers on thermal degradation and fire performance of epoxy-based intumescent coating for fire protection of steel substrate. Prog Org Coat 132:148–158
53. Li B, He C, Lu W, Wang J, Zeng Y, Gao B (2019) Synthesis of highly branched polymethylphenylsiloxane grafted epoxy resin copolymer for high efficiency ablation thermal protection coating. Prog Org Coat 126:178–186
54. Sun H, Lei F, Li T, Han H, Li B, Li D, Sun D (2021) Facile fabrication of novel multifunctional lubricant-infused surfaces with exceptional tribological and anticorrosive properties. ACS Appl Mater Interfaces 13(5):6678–6687